Dry reforming of methane over calcium-deficient hydroxyapatite supported cobalt and nickel catalysts

Thi Quynh Tran, Doan Pham Minh, Thanh Son Phan, Quoc Nghi Pham, Hoan Nguyen Xuan

Dry reforming of methane over calcium-deficient hydroxyapatite supported cobalt and nickel catalysts

Thi Quynh Tran [a,c], Doan Pham Minh [b,c,*], Thanh Son Phan [c], Quoc Nghi Pham [d], Hoan Nguyen Xuan [a]

[a] Faculty of Chemistry, VNU University of Science, Vietnam National University, Hanoi 110000, Viet Nam
[b] Institute of Research and Development, Duy Tan University, Da Nang 550000, Viet Nam
[c] Université de Toulouse, Mines Albi, CNRS, Centre RAPSODEE, Campus Jarlard, F-81013 Albi Cedex 09, France
[d] ICMMO (UMR 8182 CNRS), Université Paris-Sud, Université Paris-Saclay, 91405 Orsay, France

HIGHLIGHTS

- Hydroxyapatites (HAP) were successfully synthesized from different precursors.
- Co/HAP catalysts were systematically more active than Ni/HAP catalysts.
- No synergetic effect of bimetallic Ni-Co/HAP catalysts could be found.
- Calcium-deficient HAP favors the catalytic stability of Co- and Ni-based catalysts.

GRAPHICAL ABSTRACT

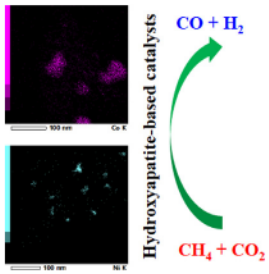

ABSTRACT

Calcium-deficient hydroxyapatite (HAP) non-porous supports were synthesized from $Ca(NO_3)_2$ and $NH_4H_2PO_4$ (conventional synthesis route, HAP_N support) and from $CaCO_3$ and H_3PO_4 (new synthesis route, HAP_C support) by wet chemical precipitation method. Monometallic and bimetallic supported catalysts were prepared by incipient wetness impregnation using $Co(NO_3)_2$ and $Ni(NO_3)_2$ salts. The size of Co- and Ni-based particles varied from some nm to dozens nm. Dry reforming of methane (DRM) tests at 700 °C, and 1.6 bar shows that HAP-supported cobalt catalysts were systematically more active than HAP-supported nickel catalysts, which is a new finding in DRM. Increasing the molar ratio of Ca/P from 1.43 (HAP_N) to 1.60 (HAP_C) support led to a slight decrease of the catalytic activity but an improvement of the catalytic stability. Thus, HAP_C support synthesized from $CaCO_3$ and H_3PO_4 is a good candidate for designing an efficient catalyst for the DRM reaction.

Keywords:
Dry reforming of methane
Cobalt
Nickel
Hydroxyapatite
Supported catalyst
Syngas

1. Introduction

Dry reforming of methane (DRM) allows converting methane and carbon dioxide, known as two main greenhouse gases, into synthetic gas (syngas, a mixture of carbon monoxide and hydrogen) which is a versatile gas platform for the synthesis of various chemicals and fuels (Abdulrasheed et al., 2019; Liu et al., 2010; Zhu et al., 2020). Research has been devoted to DRM during the last decades, but to date, there is not industrial deployment yet (Abdullah et al., 2017; Abdulrasheed et al., 2019; Şener et al., 2018; Usman et al., 2015). This process needs high temperature (above 700 °C) and atmospheric pressure to theoretically reach high conversion and high syngas selectivity (Abdulrasheed et al., 2019; Pham Minh et al., 2018, 2013). A solid catalyst is also required to get exploitable kinetic. However, under atmosphere rich in methane and high temperature, DRM catalyst is usually deactivated by thermal sintering and the formation of solid carbon and coke (Abdulrasheed et al., 2019; Aramouni et al., 2018; Aziz

* Corresponding author.
E-mail addresses: phamminhdoan@duytan.edu.vn, doan.phamminh@mines-albi.fr (D. Pham Minh).

et al., 2019; Jang et al., 2019; Şener et al., 2018; Usman et al., 2015). The development of an active, selective, and stable catalyst currently constitutes a main scientific challenge for DRM.

Hydroxyapatite ($Ca_{10}(PO_4)_6(OH)_2$, HAP) has interesting physicochemical properties of catalyst support, e.g., possible high specific surface area and porosity, controlled acido-basicity, high thermal stability (Boukha et al., 2020; Chang et al., 2020; Pham Minh et al., 2013a). Surprisingly, it is much less studied than other conventional supports like alumina, silica, titania, zirconia, ceria, zeolite, etc. A rare review on hydroxyapatite in heterogeneous catalysis was recently done (Fihri et al., 2017). In DRM, only the works from Boukha's research team (Boukha et al., 2007, 2018; Boukha et al., 2018) and from our team (Phan et al., 2018; Rego De Vasconcelos et al., 2016; Rego de Vasconcelos et al., 2018, 2019) could be identified. HAP-based catalysts were found to be competitive versus those prepared with conventional supports such as Al_2O_3 and $MgAl_2O_4$ (Rego de Vasconcelos et al., 2019). In most cases, HAP was synthesized from soluble phosphate salts (e.g., NaH_2PO_4, KH_2PO_4, $NH_4H_2PO_4$) and calcium nitrate ($Ca(NO_3)_2$). The drawback of this synthesis way is related to the arduous washing step. In fact, fine HAP particles are formed which make the washing step difficult to eliminate counter ions like NO_3^-, Na^+, K^+, NH_4^+. Our previous studies have demonstrated that HAP could be synthesized from $CaCO_3$ and H_3PO_4 without washing step because no counter ion is present in the final HAP product (Pham Minh et al., 2013b). Also, in DRM, stoichiometric HAP having the molar ratio of Ca to P of 1.67 was usually used, except the recent work of Boukha et al. (2019) showing that calcium-deficient HAP (Ca/P < 1.67, acid supports) was more favorable for DRM than stoichiometric HAP (Ca/P = 1.67, acido-basic support) or calcium-surplus HAP (Ca/P > 1.67, basic support). This seems to be contradictory to the findings from the literature, where basic supports generally favor DRM reaction (Rego de Vasconcelos et al., 2019; Naeem et al., 2014; Alipour et al., 2014; Ibrahim et al., 2019).

The double objective of this study are: (i) to compare two supports synthesized from $Ca(NO_3)_2$ and $NH_4H_2PO_4$ (conventional synthesis route) and from $CaCO_3$ and H_3PO_4 (new synthesis route), and (ii) to investigate the catalytic performance of the catalysts prepared from calcium-deficient HAP supports. In fact, to the best of our knowledge, HAP synthesized from $CaCO_3$ and H_3PO_4 has never been investigated in DRM.

2. Materials and methods

2.1. Chemicals

Commercial chemicals including ammonium hydroxide solution (NH_4OH, Merck, 25–28 wt%), calcium nitrate tetrahydrate ($Ca(NO_3)_2{\cdot}4H_2O$, >99%, China), calcium carbonate ($CaCO_3$, >99%, China), ammonium dihydrogen phosphate ($NH_4H_2PO_4$, >99%, China), and phosphoric acid (85 wt.%H_3PO_4, China) were used for the synthesis of HAP supports. Nickel nitrate hexahydrate ($Ni(NO_3)_2{\cdot}6H_2O$, Fisher Scientific, >98%) and cobalt nitrate hexahydrate ($Co(NO_3)_2{\cdot}6H_2O$, Acros Organics, >98%) were used as metal precursors for and catalysts preparation. Distilled water was used as the solvent throughout the experiments.

2.2. HAP synthesis

HAP supports were synthesized by the wet chemical precipitation method at 85 °C under atmospheric pressure. For the conventional synthesis route, 400 mL of 2.5 M calcium nitrate solution was mixed with 400 mL of 1.5 M ammonium dihydrogen phosphate solution at 85 °C for 48 h under stirring and controlled pH of 8.5–10 by addition of a NH_4OH solution. A white precipitate was formed, which was separated by filtration. Then, it was washed several times with distilled water, dried at 105 °C overnight in an oven, and crushed into a fine powder. This support is thereafter called HAP_N. For the new synthesis route, 100 g of fine calcium carbonate powder was added to 800 mL of 0.75 M H_3PO_4 solution. The mixture was kept at 85 °C for 48 h under stirring and controlled pH of 8.5–10 by the addition of a NH_4OH solution. Then, the solid product was separated by filtration and dried at 105 °C overnight in an oven. This support is thereafter called HAP_C.

2.3. Catalyst preparation

The supports HAP_N and HAP_C were used for the preparation of monometallic and bimetallic supported catalysts by the conventional incipient wetness impregnation using nickel nitrate and cobalt nitrate precursors (Phan et al., 2018; Rego de Vasconcelos, 2016). Firstly, the specific porous volume of each support was determined. For monometallic catalyst preparation, an aqueous solution of nickel nitrate or cobalt nitrate was prepared and impregnated on HAP_N or HAP_C at room temperature (ca. 20 °C). Then, the mixture was dried overnight at 105 °C and calcined under the air atmosphere at 700 °C before the characterization and/or the catalytic test. The concentrations of nickel nitrate and cobalt nitrate solutions were calculated to reach the theoretical value of Ni or Co content in the final catalyst of 10 wt%. For bimetallic catalyst preparation, a solution containing both Ni and Co was used for the impregnation step. The mixture was also dried overnight at 105 °C and calcined under the air atmosphere at 700 °C before the characterization and/or the catalytic test. The theoretical value of Ni and Co content in each bimetallic catalyst is 5 wt%. The following catalysts were prepared: 10Ni/HAP_N; 10Ni/HAP_C; 10Co/HAP_N; 10Co/HAP_C; 5Ni-5Co/HAP_N; 5Ni-5Co/HAP_C.

2.4. Characterization

Ca, P, Ni, and Co contents in the supports and catalysts were determined by inductively-coupled plasma coupled with atomic emission spectroscopy (ICP-AES) using a HORIBA Jobin Yvon Ultima 2 apparatus. Prior to the measurements, solid samples were completely dissolved in *aqua regia* at 90 °C for 1 h. The specific surface area and the porosity of the supports and of the fresh catalysts were analyzed by nitrogen adsorption/desorption using a MICROMETRICS Gemini Vacprep 061. Before the analysis, the samples were pretreated at 105 °C for 24 h below 100 mbar. Powder *X*-ray diffraction (XRD) analysis was performed with a Bruker D8 Advance *X*-ray diffractometer (Cu K_α radiation at λ = 1.5418 Å; scan step size of 0.017 °s^{-1}; 2θ range of 10–70 °). Thermogravimetric analysis (TGA) and differential scanning calorimetry (DSC) was simultaneously carried out in the temperature range of 30–1200 °C (10 °C/min heating rate) under airflow (100 NmL min^{-1}) using a SDT Q600 apparatus. Used catalysts were also analyzed by TGA coupled with mass spectroscopy (TGA-MS), where a Pfeiffer Vacuum OmniStar GSD 320 apparatus was used to analyze the gas emitted by TGA apparatus. Fourier Transform Infrared Spectroscopy (FTIR) was carried out with a FTIR Jasco-6300 spectrometer (wavenumber range of 4000–400 cm^{-1}). Environmental Scanning Electron Microscopy (ESEM) analysis was performed on a Philips XL30 ESEM apparatus. Transmission electron microscopy coupled with energy-dispersive X-ray spectroscopy (TEM-EDX) analysis of fresh and spent catalysts were carried out with a FEG JEOL JEM 2100F machine, equipped with a HAADF detector.

2.5. Catalytic reaction

DRM reaction was carried out in a tubular fixed-bed ceramic reactor (8 mm inner diameter, 25 cm length). A thermocouple was set at the center of the catalyst bed to control the reaction temperature. For a given test, the reactor was firstly filled with an inert alumina powder (S_{BET} < 3 m^2/g). Then, the catalyst (340 mg) was diluted 2 times with the same alumina to improve heat dissipation inside the catalyst bed. This mixture was placed at the center of the reactor. Finally, the reactor was competed with inert alumina powder (see Fig. SI1 for illustration). Prior to the DRM reaction, the catalyst was reduced *in-situ* at 700 °C for 2 h under 4 vol% H_2/N_2 (70 NmL/min). Then, the DRM reaction started at 700 °C by feeding the reactor with a mixture of $CH_4/CO_2/N_2$ = 20/20/60 (vol.%, 180 NmL/min total gas flow rate). Under these conditions, the pressure drop inside the reactor was 0.6 bar leading to a total pressure equal to 1.6 bar. This latter was measured by a manometer. Water formed as a byproduct of the DRM reaction was quantified by a water trap. This latter is composed of a tube of silica gel. During the reaction, this tube was periodically weighed to determine the rate of water formation. The total flow rate of the dried outlet gas was measured by a gas counter, while its composition was analyzed by a μ-GC (MyGC model, Agilent).

From the composition and the total gas flow rate at the reactor outlet, the conversion and selectivity of the reaction are defined by the following equations:

$$CH_4 \text{ conversion } (X_{CH_4}, \%) : X_{CH_4} = \frac{\dot{Q}_{CH4}^{inlet} - \dot{Q}_{CH4}^{outlet}}{\dot{Q}_{CH4}^{inlet}} \times 100 \quad (1)$$

$$CO_2 \text{ conversion } (X_{CO_2}, \%) : X_{CO_2} = \frac{\dot{Q}_{CO2}^{inlet} - \dot{Q}_{CO2}^{outlet}}{\dot{Q}_{CO2}^{inlet}} \times 100 \quad (2)$$

$$CO \text{ selectivity } (S_{CO}, \%) : S_{CO} = \frac{\dot{Q}_{COformed}}{2 \times (\dot{Q}_{CO2}^{inlet} - \dot{Q}_{CO2}^{outlet})} \times 100 \quad (3)$$

$$H_2 \text{ selectivity } (S_{H_2}, \%) : S_{H_2} = \frac{\dot{Q}_{H2formed}}{2 \times (\dot{Q}_{CH4}^{inlet} - \dot{Q}_{CH4}^{outlet})} \times 100 \quad (4)$$

$$H_2O \text{ selectivity } (S_{H_2O}, \%) : S_{H_2O} = \frac{\dot{Q}_{H2formed}}{2 \times (\dot{Q}_{CO2}^{inlet} - \dot{Q}_{CO2}^{outlet})} \times 100 \quad (5)$$

Solid carbon and coke selectivity (S_C, %):

$$S_C = \frac{\dot{Q}_c}{\left(\dot{Q}_{CH4}^{inlet} - \dot{Q}_{CH4}^{outlet}\right) + \left(\dot{Q}_{CO2}^{inlet} - \dot{Q}_{CO2}^{outlet}\right)} \times 100 \quad (6)$$

where $\dot{Q}_{CH4}^{inlet}$: CH_4 inlet flow rate (mmol/min); $\dot{Q}_{CH4}^{outlet}$: CH_4 outlet flow rate (mmol/min); $\dot{Q}_{CO2}^{inlet}$: CO_2 inlet flow rate (mmol/min); $\dot{Q}_{CO2}^{outlet}$: CO_2 outlet flow rate (mmol/min); $\dot{Q}_{COformed}$: CO outlet flow rate (mmol/min); $\dot{Q}_{H2formed}$: H_2 outlet flow rate (mmol/min); $\dot{Q}_{H2formed}$: H_2O outlet flow rate (mmol/min); $\dot{Q}_c$: solid carbon outlet flow rate (mmol/min), which is calculated by difference between inlet carbon (under the form of CH_4 and CO_2) and outlet carbon analyzed (CH_4, CO_2 and CO).

As previously defined, solid carbon is formed from CO disproportionation, while coke is formed by decomposition and condensation of hydrocarbons (methane in DRM) (Bartholomew, 1982). In this work, it is not evident to distinguish solid carbon and coke, which are accumulated in the catalyst bed. Thus, only the total selectivity into solid carbon and coke (S_C) is calculated according to Eq. (6).

3. Results

3.1. Supports and fresh catalysts characterization

3.1.1. ICP-AES

ICP-AES analysis results are presented in Table 1. The HAP_N support had a low molar ratio of Ca/P of 1.43, indicating the formation of a calcium-deficient HAP. On the other hand, the molar ratio of Ca/P in HAP_C support was 1.60, which is close to the Ca/P ratio of the stoichiometric HAP (1.67). For Ni and Co contents, the results obtained by ICP-AES analysis were close to the theoretical values (10 wt% for monometallic catalysts and 5 wt% of Ni and 5 wt% of Co for bimetallic catalysts). In reality, some amounts of Ni and Co could be lost during the impregnation (e.g., amounts stuck on flask walls) (Rego De Vasconcelos et al., 2016).

3.1.2. Nitrogen adsorption-desorption isotherms

Nitrogen adsorption-desorption isotherms of the initial supports and fresh calcined catalysts are presented in Fig. 1. According to the IUPAC classification (Thommes et al., 2015), both the initial supports had the type III profile of non-porous or macro-porous materials (Fig. 1 a). From these isotherms, the specific surface area of the supports and fresh catalysts could be calculated by the BET method (S_{BET}), and the results are shown in Table 1. The specific surface area is relatively low, which indicates the formation of non-porous materials. For DRM reaction, low specific surface area as the result of the absence of pores in the synthesized HAP supports could be an advantage because it limits the thermal sintering of the support during the chemical reaction at high temperature. In fact, Rego de Vasconcelos et al. (2018) tried to reduce the specific surface area of stoichiometric HAP support before nickel deposition to avoid thermal sintering during the DRM reaction. They found that the Ni catalyst prepared with sintered HAP support was stable at 700 °C. Also, the absence of porosity could limit the formation of "cold-spot" inside catalyst bed (Chen et al., 2012).

The supported catalysts (Fig. 1b) showed the similar isotherms of non-porous materials compared to the initial supports. The catalysts were prepared by incipient wetness impregnation, which is known as a soft preparation method without a notable impact on the surface of HAP supports (Rego de Vasconcelos, 2016).

3.1.3. FTIR

The FTIR spectra of the two supports and fresh calcined catalysts are presented in Fig. 2. Both supports mostly showed vibration peaks of orthophosphate (PO_4^{3-}, peaks at 1090, 1035, 963, 606, 569, and 473 cm^{-1}) and hydroxyl (OH^-, peaks at 3572 and 632 cm^{-1}) groups (Elliott, 1994; Pham Minh et al., 2012). For HAP_N, a weak vibration peak appeared at 876 cm^{-1}, which is not present in the stoichiometric HAP. According to McGrellis et al. (2001), this peak could be attributed to the vibration of the P-O bond in HPO_4^{2-} groups of calcium-deficient HAP. For HAP_C, carbonate groups (CO_3^{2-}) were inserted inside the apatitic structure of this support, characterized by the peaks at 1454, 1412 et 872 cm^{-1} (A-type carbonated hydroxyapatite where CO_3^{2-} groups replace OH^-groups), and at 1545 and 872 cm^{-1} (B-type carbonated hydroxyapatite where CO_3^{2-} groups replace PO_4^{3-} groups) (Antonakos et al., 2007; Wilson et al., 2004). The deposition of Ni and Co (Fig. 2b) did not lead to notable modification of FTIR signals compared to those of the initial supports (Fig. 2a).

Table 1
ICP-AES analysis and specific surface area of the supports and fresh catalysts.

Support, catalyst	Ni (wt.%)	Co (wt, %)	Molar ratio, Ca/P	S_{BET} (m^2/g)
HAP_N	–	–	1.43	15
10Ni/HAP_N	8.7	–	1.37	8
10Co/HAP_N	–	8.2	1.40	7
5Ni-5Co/HAP_N	4.4	4.7	1.43	8
HAP_C	–	–	1.60	6
10Ni/HAP_C	8.6	–	1.60	5
10Co/HAP_C	–	9.1	1.59	6
5Ni-5Co/HAP_C	4.5	4.8	1.58	6

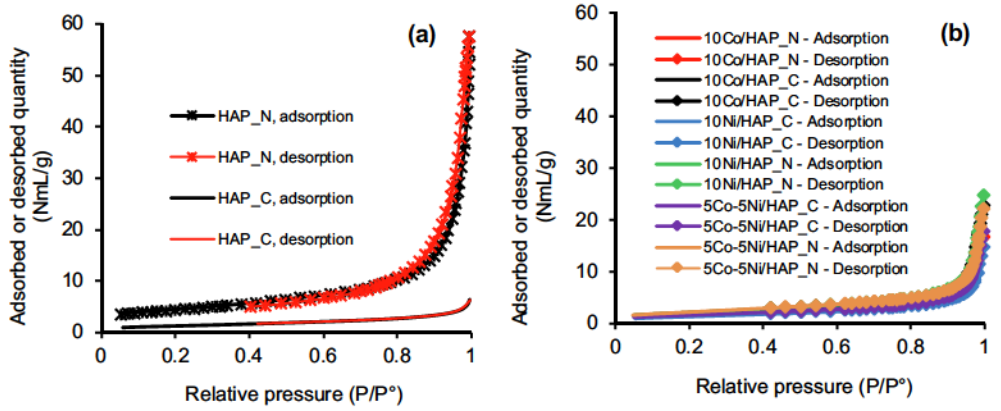

Fig. 1. Nitrogen adsorption-desorption isotherms of the supports (a) and fresh catalysts (b).

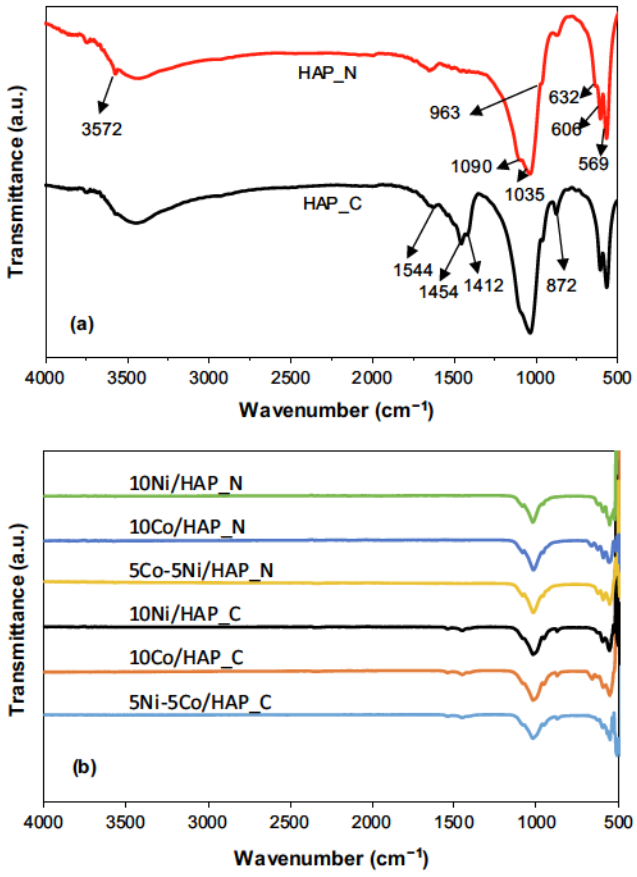

Fig. 2. FTIR spectra of the HAP supports (a) and fresh calcined catalysts (b).

3.1.4. TG analysis

The thermal behavior of the supports is shown in Fig. 3. The HAP_N support with the Ca/P molar ratio of 1.43 had several mass losses at 30–700 °C. For this kind of calcium-deficient HAP, protons (H^+) are present in the apatitic structure, as evidenced by FTIR analysis (HPO_4^{2-} groups) in Fig. 2 and XRD analysis (dicalcium phosphate dihydrate) in Fig. 4. Dehydration reaction could take place according to Eqs. (7)–(9) (Elliott, 1994). The next mass losses above 700 °C could be due to the decarbonation of carbonated hydroxyapatite formed by the insertion of carbonate into the apatitic structure during the synthesis or the contact of HAP_N powder with the air (El Feki et al., 1994; Tonsuaadu et al., 1995; Yao et al., 2009), as well as the long dehydration of hydroxyl groups at high temperature (Sofronia et al., 2014). All these dehydrations were endothermal (*DSC signals not shown*).

$$\text{Around } 110\,^{\circ}\text{C}: Ca(H_2PO_4)_2 \cdot H_2O \rightarrow Ca(H_2PO_4)_2 + H_2O \qquad (7)$$

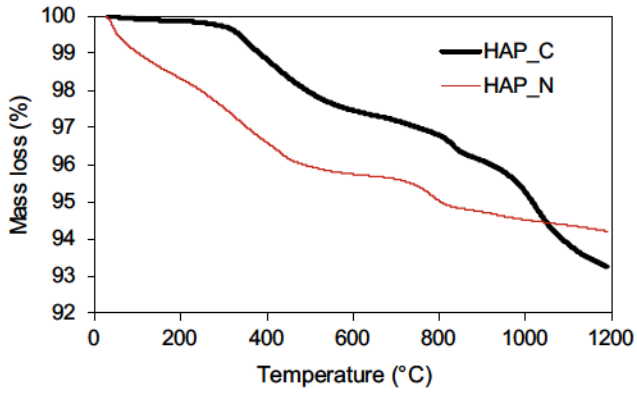

Fig. 3. TG curves of HAP_C and HAP_N.

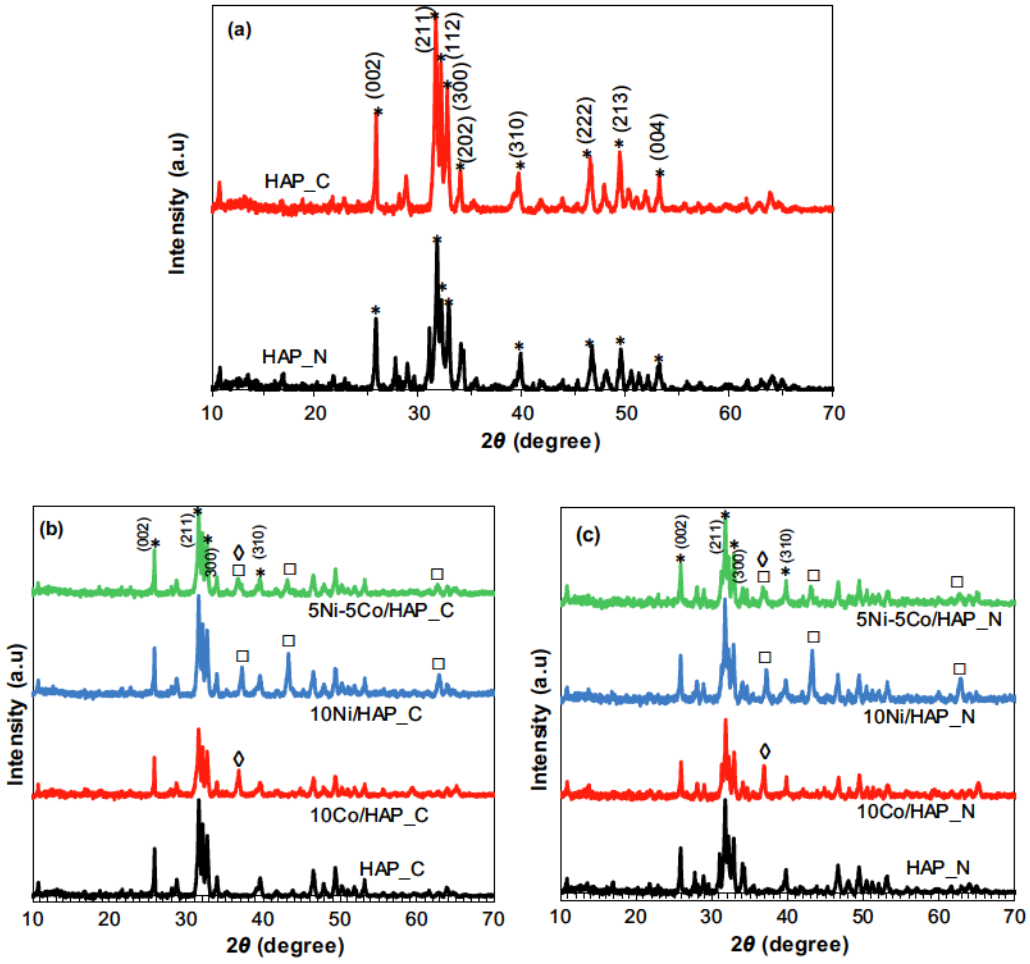

Fig. 4. XRD patterns of supports (a) and fresh calcined catalysts (b and c); Main diffraction peaks of HAP (*), Co_3O_4 (◇); and NiO (□).

$$\text{Around } 190\,^{\circ}\text{C}: CaHPO_4 \cdot 2H_2O \rightarrow CaHPO_4 + 2H_2O \quad (8)$$

$$\text{Around } 430\,^{\circ}\text{C}: 2CaHPO_4 \rightarrow Ca_2P_2O_7 + H_2O \quad (9)$$

The Ca/P molar ratio of HAP_C support was equal to 1.60. So, it must contain less protons and hydrated compounds than HAP_N. This explains its negligible mass loss before 300 °C. From 300 to 900 °C, its thermal behavior was comparable to that of HAP_N. Then, above 900 °C, a strong mass loss took place, which could be due to the dehydration of hydroxyl groups, but also the decarbonation of carbonated hydroxyapatite as previously observed (Pham Minh et al., 2014). TG results evidenced that carbonated hydroxyapatite content was higher in HAP_C than HAP_N, which is consistent because, during the synthesis of HAP_C, carbonic gas was formed inside the reaction medium from the decarbonation of calcium carbonate (Pham Minh et al., 2012, 2013b).

3.1.5. XRD analysis

Fig. 4a shows the XRD patterns of the supports. As expected, both supports had the apatitic structure (Reference ICSD # 26204, space group P $6_3/m$ (N° 176)) with the typical diffraction peaks at 2θ angle of 25.9, 31.8, 32.2, 32.9, 46.8 and 49.7° (Elliott, 1994; Pham Minh et al., 2012; Phan et al., 2018; Sudarsanan and Young, 1969). Other compounds including carbonate apatite, octacalcium bis(hydrogenphosphate) tetrakis(phosphate) pentahydrate (OCP, $Ca_8(HPO_4)_2(PO_4)_4{\cdot}5H_2O$) and dicalcium phosphate dihydrate (DCPD, $CaHPO_4{\cdot}2H_2O$) could also be present at low contents, as previously observed (Pham Minh et al., 2012, 2013c).

Fig. 4b and c show the XRD patterns of the fresh calcined catalysts. About the support, no modification could be detected by XRD after metals deposition. HAP was found as the principal crystalline phase of all the catalysts. For the active phase of these calcined catalysts, nickel and cobalt oxides are expected. It is important to recall that their content is relatively low (theoretically 10 wt% and lower), and consequently, only major peaks of XRD patterns are indexed. For monometallic catalysts, peaks of NiO (reference ICSD # 92127 with the principal peaks at 37.2, 43.2, and 63°) or Co_3O_4 (reference ICSD # 69365 with principal peak at 36.8°) could be observed as results of the thermal decomposition of nickel nitrate and cobalt nitrate (Živković et al., 1998; Pham Minh et al., 2013a, 2013b, 2013c). For each bimetallic catalyst, crystalline diffraction peaks of both NiO and Co_3O_4 could be observed. Using the Scherrer equation (Patterson, 1939), the crystallite size of NiO or Co_3O_4 in the prepared catalysts could be estimated, which reached around 22–25 nm.

3.1.6. SEM analysis

The textural properties of the supports and the calcined catalysts are illustrated in Fig. 5. Initial supports HAP_N and HAP_C were composed of agglomerates made from micrometric primary particles of calcium phosphates. The morphology was different from each other. HAP_N was likely constituted by spherical or polygonal particles while HAP_C mostly contained prolonged flat particles having high shape factor. It could be due to the impact of the Ca/P molar ratio of these supports, but also the nature of cal-

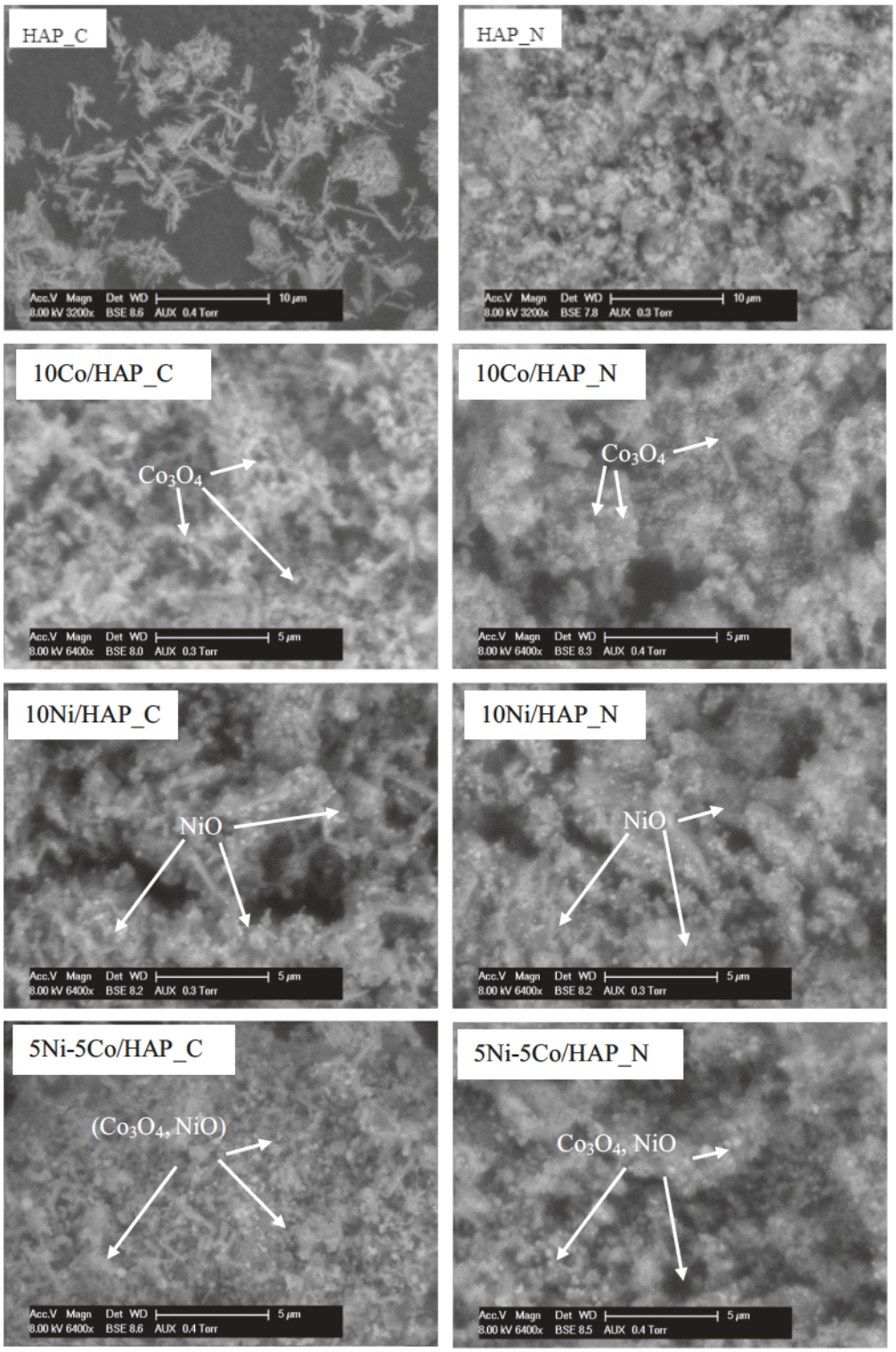

Fig. 5. SEM images of the initial supports and fresh calcined catalysts.

cium precursor in HAP synthesis (Eslami et al., 2010; Guo et al., 2013; Mondal et al., 2016; Pham Minh et al., 2012).

For calcined catalysts, NiO and Co_3O_4 particles could be observed on the surface of all the catalysts by contrast difference. At high magnification, particle size could be estimated at around dozens nm, as previously observed by Rego de Vasconcelos et al. (2016).

3.1.7. TEM analysis

3.1.7.1. Monometallic catalysts. SEM analysis did not allow a clear observation of metallic particles. Thus, TEM-EDX was performed. In all cases, EDX analysis was carried out to build the cartography of cobalt and nickel elements on the catalyst's surface (Fig. 6). For both cobalt-based catalysts (Fig. 6a–d), cobalt oxide particles of dozens nm were formed on the HAP support surface. For nickel-

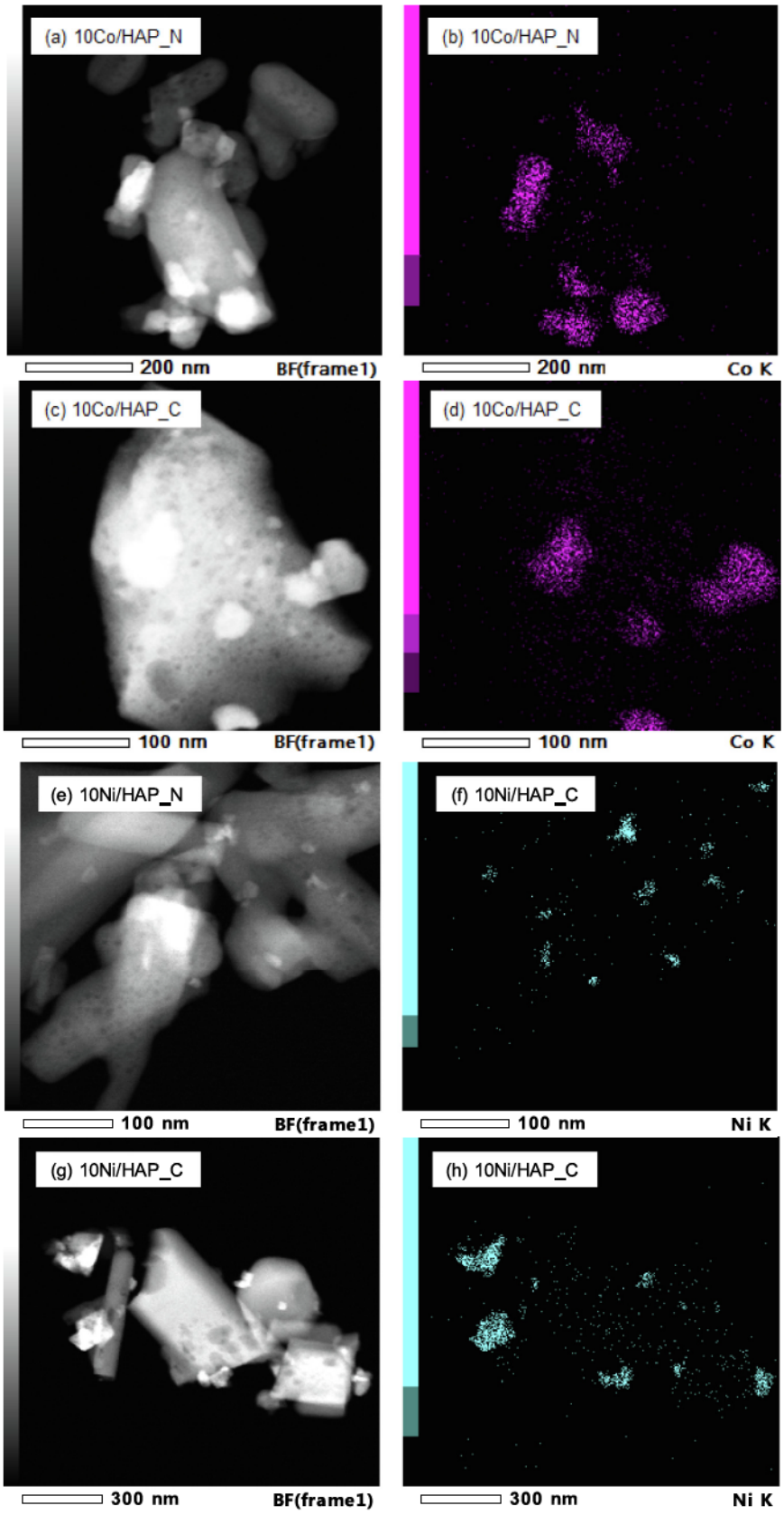

Fig. 6. TEM-EDX analysis of the fresh calcined monometallic catalysts.

based catalysts (Fig. 6e–h), the size of nickel oxide particles seemed to vary in a large range from some nm to dozens nm. Agglomerates of nickel-based particles larger than 100 nm could also be observed (see SI 2). Large nickel oxide and cobalt oxide particles formed on HAP surface by incipient wetness impregnation were already reported in the literature (Rego De Vasconcelos et al., 2018, 2019).

3.1.7.2. Bimetallic catalysts. TEM-EDX results of the bimetallic catalysts are presented in Fig. 7. As expected, bimetallic catalysts were formed under the form of nanoparticles mainly composed of Ni-Co. This was already observed for Ni-Co catalysts prepared with commercial HAP (Phan et al., 2018). The size of these nanoparticles was mostly below 50 nm, but aggregates larger than 100 nm could also be observed (see SI 3 and SI 4).

3.2. Catalytic performance

3.2.1. Methane and carbon dioxide conversion

Fig. 8 presents methane and carbon dioxide conversions in the DRM reaction over the catalysts prepared in this work at 700 °C and 1.6 bar. For the catalysts prepared with the HAP_C support, 5Ni-5Co/HAP_C was active with perfect catalytic stability during 50 h of reaction. Surprisingly, the catalytic activity of 10Ni/HAP_C increased with the reaction time. The repeatability of the DRM reaction was checked, which confirmed this catalytic behavior. Before the reaction, the catalyst was already reduced *in-situ* at 700 °C under 4 vol% H_2/N_2, which must be enough to completely reduce nickel oxides into metallic nickel, according to Rego De Vasconcelos et al. (2018). It could be supposed that a reorganization of the surface structure of this catalyst took place. Whisker carbon is usually formed during the DRM reaction using a nickel-based catalyst leading to the formation of a new catalyst surface (Abdulrasheed et al., 2019; Bartholomew, 1982; Helveg et al., 2011; Rego De Vasconcelos et al., 2018). In this case, nickel particles could be kept on the top of carbon nanofibers and thus are available and active in the DRM reaction. Another reason to explain the increase of the activity of 10Ni/HAP_C could be related to the activation of Ni^{2+} cations, inserted to the apatitic structure of HAP_C support during the impregnation step. When a HAP powder is set in contact with an aqueous solution containing bivalent metals such as Ni^{2+}, the latter could be integrated into the apatitic structure of HAP (Nguyen Thanh et al., 2018; Vahdat et al., 2019). Under the reducing atmosphere DRM reaction, these Ni^{2+} cations could be reduced to form new metallic nickel particles which are active in DRM. To confirm this hypothesis, further specific characterizations such as XPS, should be performed. Finally, 10Co/HAP_C showed a conventional catalytic profile of a supported metal catalyst, with an initial catalyst deactivation during around 20 first hours of time-on-stream. Its catalytic activity became stable during the last 30 h of reaction.

For the catalysts prepared with the HAP_N support, the conventional catalytic behavior could be observed. 10Co/HAP_N showed the highest catalytic activity. But its activity continuously decreased during 50 h of time-on-stream for methane conversion. Both 5Ni-5Co/HAP_N and 10Ni/HAP_N catalysts showed similar catalytic behavior, but their activity was smaller than that of 10Co/HAP_N.

As previously mentioned, Boukha et al. (2019) found that Ni catalysts supported on calcium-deficient HAP was more active than Ni catalysts supported on stoichiometric HAP or calcium-surplus HAP. In the present work, the comparison of methane conversion during the last 30 h of time-on-stream shows that HAP_N-based catalysts (Ca/P molar ratio of 1.43) were systematically more active than HAP_C-based catalysts (Ca/P molar ratio of 1.60). This enhanced the findings of Boukha et al. (2019). However, the catalysts prepared on HAP_C were more stable than those prepared on HAP_N. The latter, with a small molar ratio of Ca/P of 1.43, must be a strongly-acidic support, which generally favors solid carbon and coke formation. Taking into account both the activity and stability of the studied catalysts, HAP_C seemed to be better than HAP_N to design a performing catalyst in the DRM reaction.

Nickel is usually reported in the literature as the best transition metal for DRM reaction (Abdulrasheed et al., 2019; Aramouni et al., 2018; Aziz et al., 2019; Gao et al., 2018; Jang et al., 2019; Pham Minh et al., 2013a). However, the results of the present study showed that when using HAP-based support, cobalt-based catalysts were more active than nickel-based catalysts. According to the results in Fig. 8, the classification of methane conversion during the last 30 h of time-on-stream could be classified by the following decreasing order: 10Co/HAP_N > 10Co/HAP_C > 5Ni-5Co/HAP_N > 5Ni-5Co/HAP_C > 10Ni/HAP_C > 10Ni/HAP_N. This is a new finding for cobalt- and nickel-supported catalysts prepared with calcium-deficient HAP support in DRM reaction.

The combination of Co and Ni in bimetallic catalysts using calcium-deficient hydroxyapatite supports seemed to do not lead to any synergetic effect in the DRM reaction. Further characterizations, such as the determination of the density of acido-basic sites of these catalysts by temperature-programmed desorption (TPD), would be useful to better understand these catalytic results.

For all six catalysts, carbon dioxide conversion was systematically higher than methane conversion. This is explained by the reverse water-gas-shift reaction (RWGS) where carbon dioxide reacts with hydrogen to form carbon monoxide and water (Aramouni et al., 2018; Aziz et al., 2019; Jang et al., 2019; Phan et al., 2018; Rego de Vasconcelos et al., 2018, 2019). The analysis of the products of the reaction will evidence the presence of this side reaction.

Porous supports with the high specific surface area are generally advantageous in heterogeneous catalysis, which allows a good dispersion of the active phase. However, in this study, the catalysts prepared with non-porous HAP supports showed high catalytic performance. In fact, DRM is a strongly-endothermal reaction, so heat transfer is an important parameter (Chen et al., 2012). The localization of active sites on the external surface of HAP particles, as highlighted by TEM-EDX analysis, is advantageous to avoid “cold-spot” (Chen et al., 2012) compared to conventional porous supports. In addition, DRM needs a high temperature (700 °C in this study), which can lead to thermal sintering of supports, in particular for those having high specific surface areas. Non-porous HAP with low specific surface areas used in this work could be advantageous to limit thermal sintering, as previously found by Rego de Vasconcelos (2016). Finally, HAP is well known for its exceptional capacity of cation exchange (Ivanets et al., 2019). Bivalent cations such as Ni^{2+} and Co^{2+} can be inserted into the first layers of HAP surface structure (Gupta et al., 2012; Ivanets et al., 2019; Nguyen Thanh et al., 2018; Smiciklas et al., 2006), leading to strong metal-support interaction between Ni and Co particles and HAP support Rego de Vasconcelos et al., 2018). This enhances the stability of HAP-based catalysts against the thermal sintering of metal nanoparticles.

3.2.2. Hydrogen and carbon monoxide selectivity

Hydrogen and carbon monoxide are expected as the two main products of the DRM reaction. This is confirmed in Fig. 9. Carbon monoxide selectivity was stable around 85% along the reaction for all the catalysts tested. On the other hand, hydrogen selectivity varied with the catalysts. Generally, the catalyst with high selectivity also showed high hydrogen selectivity. In all cases, hydrogen selectivity did not exceed 73% because of the presence of the RWGS reaction. Thus, the molar ratio of H_2/CO was smaller than the unit for all the catalysts tested. This was usually observed in the litera-

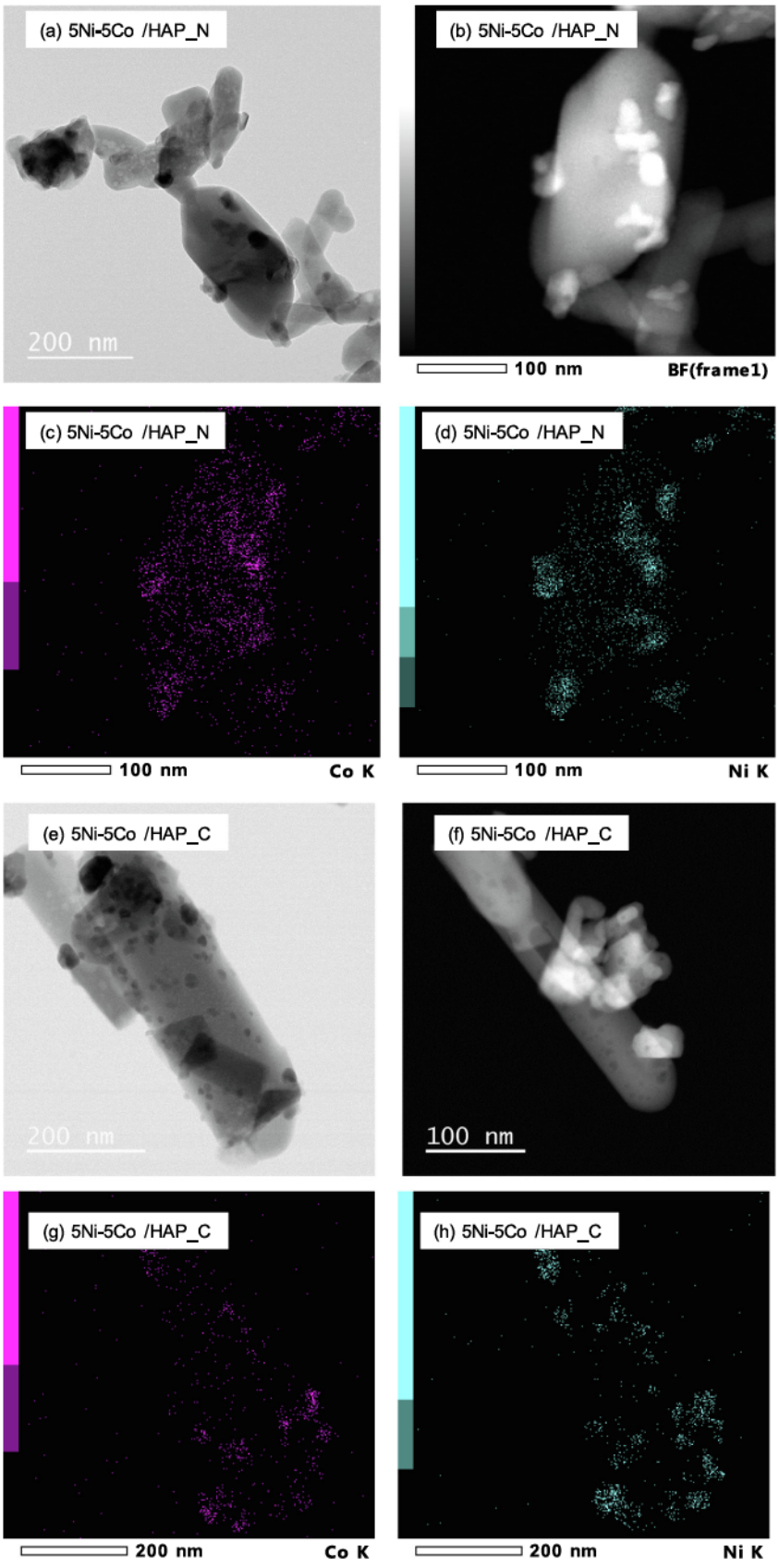

Fig. 7. TEM-EDX analysis of the fresh calcined bimetallic catalysts.

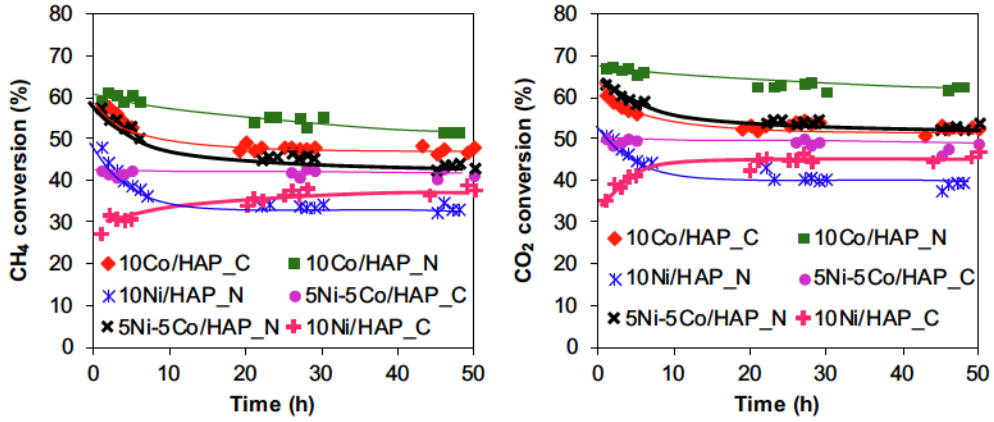

Fig. 8. Methane and carbon dioxide conversion in DRM reaction over HAP_C and HAP_N supported Ni and/or Co catalysts at 700 °C and 1.6 bar.

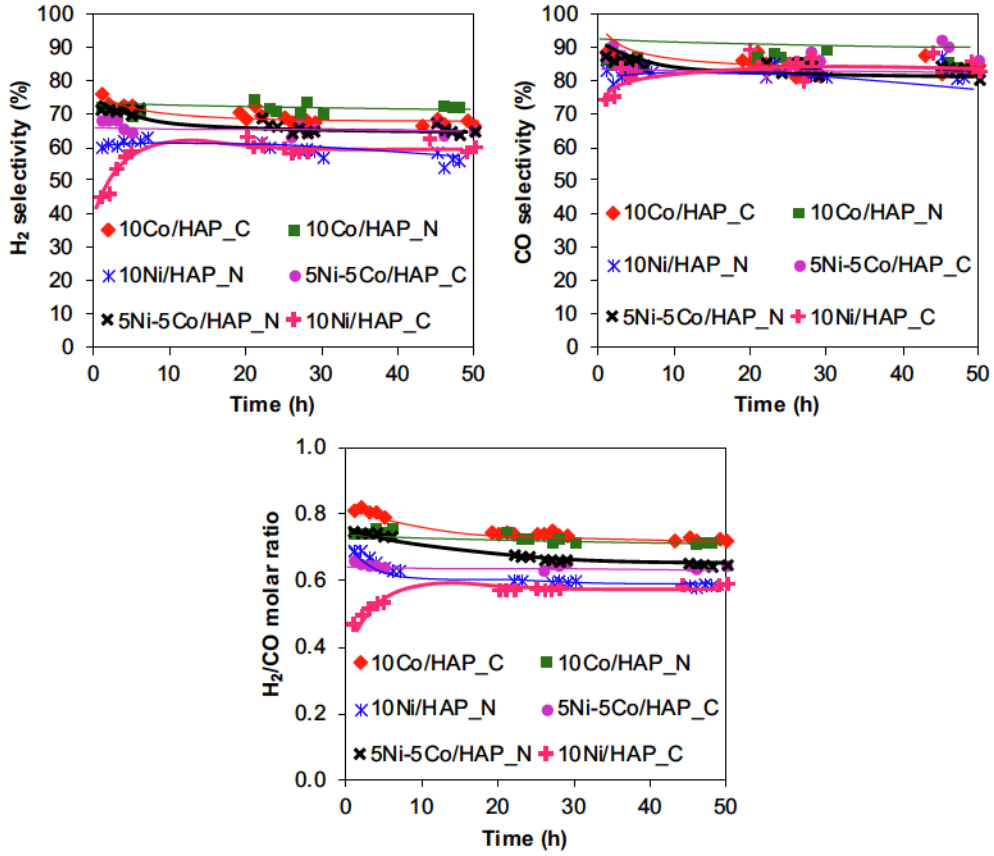

Fig. 9. Hydrogen and carbon monoxide selectivity in DRM reaction over HAP_C and HAP_N supported Ni and/or Co catalysts at 700 °C and 1.6 bar.

ture (Abdulrasheed et al., 2019; Boukha et al., 2019; Phan et al., 2018; Rego De Vasconcelos et al., 2016, 2018, 2019).

3.2.3. By-products selectivity

Water and solid carbon and coke were usually reported in the literature as the two major by-products of the DRM reaction (Abdulrasheed et al., 2019). However, to the best of our knowledge, our team seemed to be the first and the only working on the experimental quantification of water formed during the DRM reaction. Water selectivity was mostly found in the range of 10–16 %. The higher the methane conversion, the lower the water selectivity is, as previously observed (Phan et al., 2018; Rego de Vasconcelos et al., 2019). Both 10Co/HAP_N and 10Co/HAP_C showed the lowest water selectivity at around 10% along with the reaction.

The formation of solid carbon and coke in DRM reaction is inevitable from the thermodynamic point of view (Abdulrasheed et al., 2019; Aziz et al., 2019; Gao et al., 2018; Jang et al., 2019; Pham Minh et al., 2018, 2020; Rego de Vasconcelos et al., 2018). For all the catalysts investigated, solid carbon and coke selectivity was found in the range of around 8–15% (Fig. 10). Two catalysts 10Ni/HAP_C and 5Ni-5Co/HAP_C showed the lowest solid carbon and coke selectivity, explaining their good catalytic stability in Fig. 8. The catalyst 10Co/HAP_N, which had the highest methane conversion, also showed low solid carbon and coke selectivity, so its catalytic deactivation observed in Fig. 8 could be due to the

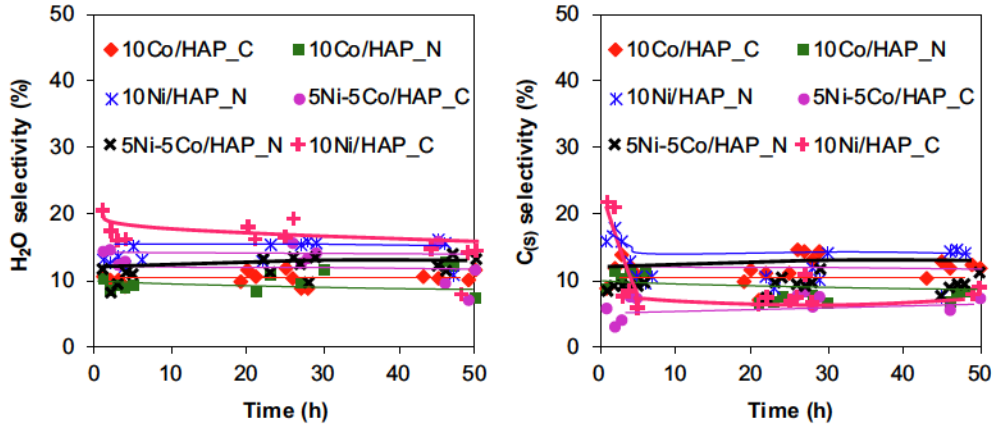

Fig. 10. Water and solid carbon and coke selectivity ($C_{(s)}$) in DRM reaction over HAP_C and HAP_N supported Ni and/or Co catalysts at 700 °C and 1.6 bar.

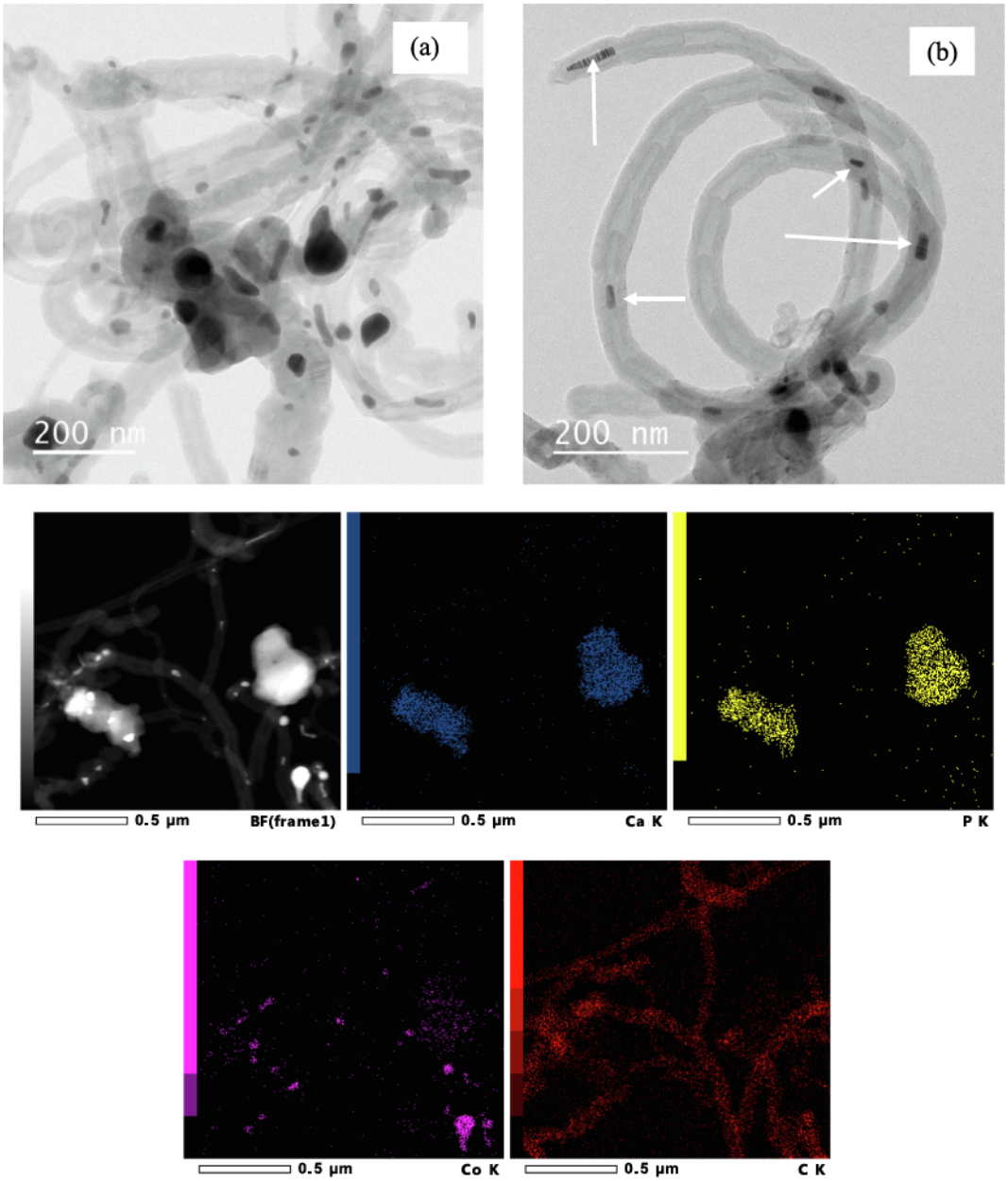

Fig. 11. TEM-EDX analysis of 10Co/HAP_N after DRM reaction at 700 °C and 1.6 bar. Arrows: encapsulated Co particles.

encapsulation of Co particles, as previously reported (Boukha et al., 2019). In fact, TEM analysis of 10Co/HAP_N recovered after DRM reaction (Fig. 11) clearly showed the encapsulation of Co nanoparticles, which could partially prevent the contact of these particles with the reactants, and also could lead to mass transfer limit by confinement effect. Also, the size of Co particles seemed to increase by thermal sintering and could partially contribute to the initial deactivation of this catalyst.

In order to evidence the nature of solid carbon and coke formed on the surface of the catalysts investigated, TG-MS analysis was performed for the used catalysts, recovered after DRM reaction. The results are presented in Fig. 12 and SI 5. Because the catalyst was diluted with inert alumina powder, it was not possible to separate catalyst particles from alumina particles. In this case, TG-MS could not be used to quantify mass losses.

In Fig. 12, all the six used catalysts showed a common mass loss with a peak around 110 °C, which could be assigned to the elimination of surface humidity. Then, a very small mass gain took place around 360–460 °C, which must be due to the re-oxidation of metallic Ni and Co into nickel oxide and cobalt oxide, respectively. During the DRM reaction, the catalyst was kept under the reducing atmosphere of syngas at 700 °C. Thus, the active phase must be reduced to the metallic state. The mass gain is not clearly observed on DTG curves but could be observed on TG curves (see Fig. SI 5). Then, between 380 and 760 °C, various mass losses took place due to the oxidation of carbon species. According to Abdulrasheed et al. (2019), coke could be formed by the decomposition of methane (in the case of DRM) causing catalyst deactivation by encapsulation of the active phase, and physisorption and/or chemisorption on the active phase; while solid carbon could

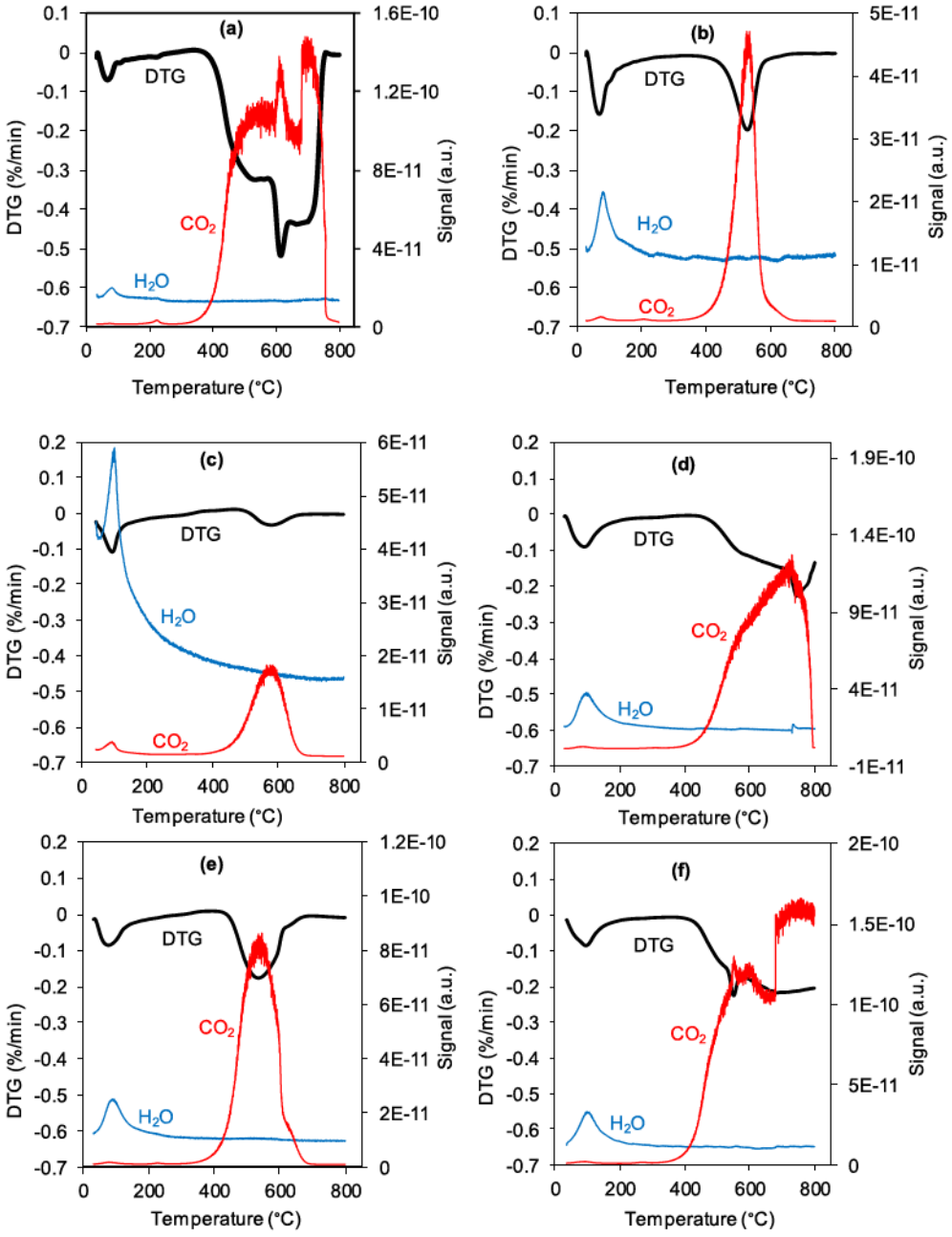

Fig. 12. TG-MS analysis of the used catalysts recovered after DRM reaction at 700 °C and 1.6 bar. DTG: derivative of TG values against time (%/min); (a) 10Co/HAP_C; (b) 10Co/HAP_N; (c) 10Ni/HAP_C; (d) 10Ni/HAP_N; (e) 5Ni-5Co/HAP_C; (f) 5Ni-5Co/HAP_N. The intensity of CO_2 and H_2O (a.u.: arbitrary unit) recorded by MS are displayed on the y-axis in the right-hand-side of each figure.

be formed from CO disproportionation. The later could start by the dissociation of CO on the surface of Ni and Co nanoparticles to form atomic adsorbed carbon species named C_α. Then, C_α species could react together to form polymeric carbon filaments named C_β. At high temperatures, both C_α and C_β are reactive to form graphitic carbon named C_γ, which is less active. The oxidation temperature of these carbon species is classified by the following increasing order: $C_\alpha < C_\beta < C_\gamma$ (Alia et al., 2020). In our case, the TG-MS results in Fig. 12 are coherent with the catalytic results obtained in Fig. 8. In fact, the catalytic deactivation was very low for two catalysts 10Ni/HAP_C and 5Ni-5Co/HAP_C (Fig. 8). Only filamentous carbon (C_β with the oxidation peak at 590 °C) is observed by TG-MS analyses of these two catalysts recovered after the DRM reaction (Fig. 12 c and e). Four other catalysts (10Co/HAP_C, 10Co/HAP_N, 10Ni/HAP_N and 5Ni-5Co/HAP_N) showed important initial catalytic deactivation (Fig. 8). TG-MS analyses of these catalysts recovered after the DRM reaction showed the presence of all three carbon species (corresponding to three oxidation peaks C_α, C_β, and C_γ), except the case of 10Co/HAP_N. The later shows only the oxidation peak of C_β due to filamentous carbon, as highlighted by TEM analysis in Fig. 11.

4. Conclusions and prospects

In this work, two HAP solid powders were prepared from $Ca(NO_3)_2$ and $NH_4H_2PO_4$ (HAP_N) and from $CaCO_3$ and H_3PO_4 (HAP_C). Both synthesis methods led to the formation of non-porous materials with a small specific surface area (S_{BET} = 6–15 m^2/g). Despite their molar ratio of Ca/P smaller than that of the stoichiometric material, both HAP_N and HAP_C supports had the crystalline structure of hydroxyapatite.

Monometallic and bimetallic catalysts were then prepared by incipient wetness impregnation method using Ni and Co as active metals, and HAP_N and HAP_C as catalyst supports. The size of Ni and Co-based nanoparticles and aggregates varied in a large range, and could reach dozens of nm. For bimetallic catalysts, nanoparticles and aggregates were systematically composed of both Ni and Co justifying the efficiency of the synthesis method of bimetallic catalysts.

The catalysts were then investigated in the dry reforming of methane at 700 °C and 1.6 bar. Among the monometallic catalysts tested, Co-based catalysts prepared on the same supports were systematically more active than Ni-based catalysts, which is a new finding of this work and could be due to a special combination of Co and HAP supports. The combination of both active metals in the bimetallic catalyst did not lead to a particular synergy effect. Finally, the catalysts prepared with HAP_N, which is a calcium-deficient material (molar ratio of Ca/P equal to 1.43), were slightly more active but less stable than those prepared with HAP_C (molar ratio of Ca/P equal to 1.60). Thus, HAP_C is found to be a good candidate to design an efficient catalyst for the DRM reaction. In all cases, water and solid carbon and coke were formed as by-products. Their elimination still constitutes the main challenge of dry reforming of methane. Future work would be focused on the optimization of the catalyst synthesis to reduce the size of metals nanoparticles, which can improve the resistance to the formation of carbon and coke.

CRediT authorship contribution statement

Thi Quynh Tran: Conceptualization, Formal analysis, Investigation, Methodology, Writing - review & editing. **Doan Pham Minh:** Conceptualization, Formal analysis, Methodology, Project administration, Supervision, Validation, Visualization, Writing - original draft, Writing - review & editing. **Thanh Son Phan:** Investigation, Writing - review & editing. **Quoc Nghi Pham:** Software, Writing - review & editing. **Hoan Nguyen Xuan:** Conceptualization, Formal analysis, Methodology, Project administration, Software, Supervision, Validation, Visualization, Writing - review & editing.

Declaration of Competing Interest

The authors declare that they have no known competing financial interests or personal relationships that could have appeared to influence the work reported in this paper.

Acknowledgments

Part of this work was carried out in the framework of the VABHYOGAZ3 project financed by ADEME (Agence de l'environnement et de la maîtrise de l'énergie), France (VABHYOGAZ3). The authors gratefully thank ADEME for the financial support, and colleagues at the RAPSODEE research center (UMR CNRS 5302) for technical help.

Appendix A. Supplementary material

Supplementary data to this article can be found online at https://doi.org/10.1016/j.ces.2020.115975.

References

Abdullah, B., Abd Ghani, N.A., Vo, D.V.N., 2017. Recent advances in dry reforming of methane over Ni-based catalysts. J. Clean. Prod. 162, 170–185.
Abdulrasheed, A., Jalil, A.A., Gambo, Y., Ibrahima, M., Hambali, H.U., Hamid, M.Y.S., 2019. A review on catalyst development for dry reforming of methane to syngas: recent advances. Renew. Sust. Ener. Rev. 108, 175–193.
Alia, S., Khader, M.M., Almarri, M.J., Abdelmoneim, A.G., 2020. Ni-based nanocatalysts for the dry reforming of methane. Catal. Today 343, 26–37.
Alipour, Z., Rezaei, M., Meshkani, F., 2014. Effect of Ni loadings on the activity and coke formation of MgO-modified Ni/Al_2O_3 nanocatalyst in dry reforming of methane. J Ener. Chem. 23, 633–638.
Antonakos, A., Liarokapis, E., Leventouri, T., 2007. Micro-Raman and FTIR studies of synthetic and natural apatites. Biomaterials 28, 3043–3054.
Aramouni, N.A.K., Touma, J.G., Tarboush, B.A., Zeaiter, J., Ahmad, M.N., 2018. Catalyst design for dry reforming of methane: analysis review. Renew. Sust. Ener. Rev. 82, 2570–2585.
Aziz, M.A.A., Setiabudi, H.D., Teh, L.P., Annuar, N.H.R., Jalil, A.A., 2019. A review of heterogeneous catalysts for syngas production via dry reforming. J. Taiwan Inst. Chem. Eng. 101, 139–158.
Bartholomew, C.H., 1982. Carbon deposition in steam reforming and methanation. Catal. Rev.: Sci. Eng. 24, 67–112.
Boukha, Z., Gil-Calvo, M., de Rivas, B., González-Velasco, J.R., Gutiérrez-Ortiz, J.I., López-Fonseca, R., 2018. Behaviour of Rh supported on hydroxyapatite catalysts in partial oxidation and steam reforming of methane: On the role of the speciation of the Rh particles. Appl. Catal. A, Gen. 556, 191–203.
Boukha, Z., González-Velasco, J.R., Gutiérrez-Ortiz, M.A., 2020. Platinum supported on lanthana-modified hydroxyapatite samples for realistic WGS conditions: On the nature of the active species, kinetic aspects and the resistance to shut-down/start-up cycles. Appl. Catal. B: Env. 270,. https://doi.org/10.1016/j.apcatb.2020.118851 118851.
Boukha, Z., Kacimi, M., Pereira, M.F.R., Faria, J.L., Figueiredo, J.L., Ziyad, M., 2007. Methane dry reforming on Ni loaded hydroxyapatite and fluoroapatite. Appl. Catal. A: Gen. 317, 299–309.
Boukha, Z., Yeste, M.P., Cauqui, M.A., González-Velasco, J.R., 2019. Influence of Ca/P ratio on the catalytic performance of Ni/hydroxyapatite samples in dry reforming of methane. Appl Catal. A, Gen. 580, 34–45.
Chen, W., Sheng, W., Cao, F., Lu, Y., 2012. Microfibrous entrapment of Ni/Al_2O_3 for dry reforming of methane: heat/mass transfer enhancement towards carbon resistance and conversion promotion. Int. J. Hydr. Ener. 37 (23), 18021–18030.
Chang, Q., Xu, W., Li, N., Xue, C., Wang, Y., Li, Y., Wang, H., Yang, J., Hu, S., 2020. Dynamic restructuring of carbon dots/copper oxide supported on mesoporous hydroxyapatite brings exceptional catalytic activity in the reduction of 4-nitrophenol. Appl. Catal. B: Env. 263,. https://doi.org/10.1016/j.apcatb.2019.118299 118299.
El Feki, H., Khattech, I., Jemal, M., Rey, C., 1994. Décomposition thermique d'hydroxyapatites carbonatées sodées. Thermochim. Acta 237, 99–110.
Elliott, J.C., 1994. Studies in Inorganic Chemistry 18: Structure and Chemistry of the Apatites and Other Calcium Orthophosphates. Elsevier, Amsterdam/London/New York/Tokyo, pp. 9–29.
Eslami, H., Solati-Hashjin, M., Tahriri, M., Bakhshi, F., 2010. Synthesis and characterization of nanocrystalline hydroxyapatite obtained by the wet chemical technique. Mat. Sci. Poland 28 (1), 5–13.

Fihri, A., Len, C., Varma, R.S., Solhy, A., 2017. Hydroxyapatite: a review of syntheses, structure and applications in heterogeneous catalysis. Coord. Chem. Rev. 347, 48–76.

Gao, Y., Jiang, J., Meng, Y., Yan, F., Aihemaiti, A., 2018. A review of recent developments in hydrogen production via biogas dry reforming. Ener. Conv. Manag. 171, 133–155.

Guo, X., Yan, H., Zhao, S., Zhang, L., Li, Y., Liang, X., 2013. Effect of calcining temperature on particle size of hydroxyapatite synthesized by solid-state reaction at room temperature. Adv. Powder Technol. 24, 1034–1038.

Gupta, N., Kushwaha, A.K., Chattopadhyaya, M.C., 2012. Adsorptive removal of Pb^{2+}, Co^{2+} and Ni^{2+} by hydroxyapatite/chitosan composite from aqueous solution. J. Taiwan Instit. Chem. Eng. 43, 125–131.

Helveg, S., Sehested, J., Rostrup-Nielsen, J.R., 2011. Whisker carbon in perspective. Catal. Today 178, 42–46.

Ibrahim, A.A., Al-Fatesh, A.S., Khan, W.U., Kasim, S.O., Abasaeed, A.E., Fakeeha, A.H., Bonura, G., Frusteri, F., 2019. Enhanced coke suppression by using phosphatezirconia supported nickel catalysts under dry methane reforming conditions. Int. J. Hyd. Ener. 44, 27784–27794.

Ivanets, A.I., Kitikova, N.V., Shashkova, I.L., Roshchina, M.Y., Srivastava, V., Sillanpää, M., 2019. Adsorption performance of hydroxyapatite with different crystalline and porous structure towards metal ions in multicomponent solution. J. Water Proc. Eng. 32,. https://doi.org/10.1016/j.jwpe.2019.100963 **100963.**

Jang, W.J., Shim, J.O., Kim, H.M., Yoo, S.Y., Roh, H.S., 2019. A review on dry reforming of methane in aspect of catalytic properties. Catal. Today 324, 15–26.

Liu, K., Song, C., Subramani, V., 2010. Hydrogen and Syngas Production and Purification Technologies. John Wiley & Sons, Hoboken, New Jersey.

McGrellis, S., Serafini, J.N., JeanJean, J., Pastol, J.L., Fedoroff, M., 2001. Influence of the sorption protocol on the uptake of cadmium ions in calcium hydroxyapatite. Sep. Purif. Technol. 24, 129–138.

Mondal, S., Dey, A., Pal, U., 2016. Low temperature wet-chemical synthesis of spherical hydroxyapatite nanoparticles and their *in situ* cytotoxicity study. Adv. Nano Res. 4, 309–321.

Naeem, M.A., Al-Fatesh, A.S., Abasaeed, A.E., Fakeeha, A.H., 2014. Activities of Ni-based nano catalysts for CO_2-CH_4 reforming prepared by polyol process. Fuel Proc. Technol. 122, 141–152.

Nguyen Thanh, D., Novák, P., Vejpravova, J., Nguyen Vun, H., Lederer, J., Munshi, T., 2018. Removal of copper and nickel from water using nanocomposite of magnetic hydroxyapatite nanorods. J. Magnetism Magnetic Mat. 456, 451–460.

Patterson, A., 1939. The Scherrer formula for X-ray particle size determination. Phys. Rev. 56, 978–982.

Pham Minh, D., Galera Martinez, M., Nzihou, A., Sharrock, P., 2013a. Thermal behaviorof apatitic calcium phosphates synthesized from calcium carbonate andorthophosphoric acid or potassium dihydrogen orthophosphate. J. Therm. Anal. Calorim. 112, 1145–1155.

Pham Minh, D., Hernandez Torres, A., Rego de Vasconcelos, B., Siang, T.J., Vo, D.V.N., 2020. Conversion of biogas to syngas via catalytic CO_2 reforming reaction: An overview of thermodynamic aspects, catalytic design and reaction kinetics. In: Nanda, S., Vo, D.V.N., Sarangi, P.K. (Eds.), Biorefinery of Alternative Resources: Targeting Green Fuels and Platform Chemicals. Springer International Publishing AG, pp. 427–456.

Pham Minh, D., Lyczko, N., Sebei, H., Nzihou, A., Sharrock, P., 2012. Synthesis of calcium hydroxyapatite from calcium carbonate and different orthophosphate sources: A comparative study. Mat. Sci. Eng. B 177, 1080–1089.

Pham Minh, D., Nzihou, A., Sharrock, P., 2014. Carbonated hydroxyapatite starting from calcite and different orthophosphates under moderate hydrothermal conditions: synthesis and surface reactivity in simulated body fluid. Mat. Res. Bull. 60, 292–299.

Pham Minh, D., Siang, T.J., Vo, D.V.N., Phan, T.S., Ridart, C., Nzihou, A., Grouset, D., 2018. Hydrogen production from biogas reforming: An overview of steam reforming, dry reforming, dual reforming, and tri-reforming of methane. In: Azzaro, C. (Ed.), Hydrogen Supply Chains – Design, Deployment and Operation. Academic Press, pp. 111–166.

Pham Minh, D., Tran, N.D., Nzihou, A., Sharrock, P., 2013b. One-step synthesis of calcium hydroxyapatite from calcium carbonate and orthophosphoric acid under moderate conditions. Ind. Eng. Chem. Res. 52, 1439–1447.

Pham Minh, D., Tran, N.D., Nzihou, A., Sharrock, P., 2013c. Carbonate-containing apatite (CAP) synthesis under moderate conditions starting from calcium carbonate and orthophosphoric acid. Mat. Sci. Eng. C 33, 2971–2980.

Phan, T.S., Sane, A.R., Rêgo de Vasconcelos, B., Nzihou, A., Sharrock, P., Grouset, D., Pham Minh, D., 2018. Hydroxyapatite supported bimetallic cobalt and nickel catalysts for syngas production from dry reforming of methane. Appl. Catal. B: Env. 224, 310–321.

Rego de Vasconcelos, B. 2016. Phosphates-based catalysts for synthetic gas (syngas) production using CH4 and CO2. PhD thesis. École Nationale Supérieure des Mines d'Albi-Carmaux (France). https://tel.archives-ouvertes.fr/tel-01365331.

Rego de Vasconcelos, B., Pham Minh, D., Martins, E., Germeau, A., Sharrock, P., Nzihou, A. 2019. Highly-efficient hydroxyapatite-supported nickel catalysts for dry reforming of methane. Int. J. Hydr. Ener. https://doi.org/10.1016/j.ijhydene.2019.08.068.

Rego de Vasconcelos, B., Pham Minh, D., Sharrock, P., Nzihou, A., 2018. Regeneration study of Ni/hydroxyapatite spent catalyst from dry reforming. Catal. Today 310, 107–115.

Rego de Vasconcelos, B., Zhao, L., Sharrock, P., Nzihou, A., Pham Minh, D., 2016. Catalytic transformation of carbon dioxide and methane into syngas over ruthenium and platinum supported hydroxyapatites. Appl. Surf. Sci. 390, 141–156.

Şener, A.N., Günay, M.E., Leba, A., Yildirim, R., 2018. Statistical review of dry reforming of methane literature using decision tree and artificial neural network analysis. Catal. Today 299, 289–302.

Smiciklas, I., Dimovic, S., Plecas, I., Mitric, M., 2006. Removal of Co^{2+} from aqueous solutions by hydroxyapatite. Water Res. 40, 2267–2274.

Sofronia, A.M., Baies, R., Anghel, E.M., Marinescu, C.A., Tanasescu, S., 2014. Thermal and structural characterization of synthetic and natural nanocrystalline hydroxyapatite. Mat. Sci. Eng. C 43, 153–163.

Sudarsanan, K., Young, R.A., 1969. Significant precision in crystal structural details. Holly Springs hydroxyapatite. Acta Crystall. B 25, 1534–1543.

Thommes, M., Kaneko, K., Neimark, A.V., Olivier, J.P., Rodriguez-Reinoso, F., Rouquerol, J., Sing, K.S.W., 2015. Physisorption of gases, with special reference to the evaluation of surface area and pore size distribution (IUPAC Technical Report). Pure Appl. Chem. 87, 1051–1069.

Tonsuaadu, K., Peld, M., Leskela, T., Mannonen, R., Niinisto, L., Veiderma, M.A., 1995. A thermoanalytical study of synthetic carbonatecontaining apatites. Thermochim. Acta. 256, 55–65.

Usman, M., Wan Daud, W.M.A., Abbas, H.F., 2015. Dry reforming of methane: Influence of process parameters-a review. Renew. Sust. Ener. Rev. 45, 710–744.

Vahdat, A., Ghasemi, B., Yousefpour, M., 2019. Synthesis of hydroxyapatite and hydroxyapatite/Fe_3O_4 nanocomposite for removal of heavy metals. Env. Nanotechnol. Monitor. Manag. 12,. https://doi.org/10.1016/j.enmm.2019.100233 **100233.**

Wilson, R.M., Elliott, J.C., Dowker, S.E.P., Smith, R.I., 2004. Rietveld structure refinement of precipitated carbonate apatite using neutron diffraction data. Biomaterials 25, 2205–2213.

Yao, F., LeGeros, J.P., LeGeros, R.Z., 2009. Simultaneous incorporation of carbonate and fluoride in synthetic apatites: effect on crystallographic and physico-chemical properties. Acta Biomat. 5, 2169–2177.

Zhu, W., Fu, J., Liu, J., Chen, Y., Li, X., Huang, K., Cai, Y., He, Y., Zhou, Y., Su, D., Zhu, J.J., Lin, Y., 2020. Tuning single atom-nanoparticle ratios of Ni-based catalysts for synthesis gas production from CO_2. Appl. Catal. B: Env. 264,. https://doi.org/10.1016/j.apcatb.2019.118502 **118502.**

Živković, Ž.D., Živković, D.T., Grujičić, D.B., 1998. Kinetics and mechanism of the thermal decomposition of $M(NO_3)_2{\cdot}nH_2O$ (M=Cu Co, Ni). J. Therm. Anal. Calor. 53, 617–623.